UNCERTAINTY QUANTIFICATION IN IMAGE SEGMENTATION FOR IMAGE-BASED ROCK PHYSICS IN A SHALY-SANDSTONE

James Howard, Sam Lin, Shawn Zhang
DigiM Solution LLC

This paper was prepared for presentation at the International Symposium of the Society of Core Analysts held in Trondheim, Norway, 27-30 August 2018

ABSTRACT

Image processing of high-resolution 3D images to create digital representation of pore micro-structures for Image-Based Rock Physics simulations remains a highly subjective enterprise, despite the seemly precision associated with improving imaging resolutions and intensive parallel computations. The decisions on how to identify pore space, both macro- and micro-pores, and various mineral components remain very much dependent upon user choices and biases. A set of shaly-sand samples with significant amount of authigenic chlorite/smectite that lines the larger pores was tested to identify uncertainty quantification (UQ) requirements associated with image-processing steps, segmentation in particular. This sandstone provides several challenges in that the dominant clay mineral lining the pores has a high surface area and cation exchange capacity, which in turn influence hydrocarbon mobility, reservoir quality, and stimulation approach. Two segmentation strategies, conventional thresholding based and artificial intelligence (AI) based, are employed with different UQ parameter space. The pore structure extracted from these different iterations is the basis of simulations of basic petrophysical properties. Upon cross-validation with measured core properties, a UQ framework is proposed to assess the differences between the different measurements from three angles: sampling, numerical and physical.

INTRODUCTION

There has been considerable recent attention on how Image-Based Rock Physics (IBRP) can reduce uncertainty in SCAL measurements by running multiple iterations of a core analysis simulation that help evaluate the relative importance of various input parameters [1] There is less discussion on how the image processing procedures contribute to the uncertainty of the calculated properties [2,3]. The importance of characterizing the connected pore space is often reduced to the distinction between using a hypothetical pore network model (PNM) of pores and throats versus only the image-based pore volume where the distinction between pores and throats is less explicit. The latter is

restricted by the image resolution where the narrowest constrictions between observed pores that fall below resolution are not always included in any transport calculations. In contrast, a PNM based on skeletonization of the image volume leads to a geometrical characterization of pore bodies with connecting throats of finite length and volume that is often constructed from information additional to the images. The non-uniqueness of PNM construction process leads to uncertainties in the subsequent simulation of transport properties that are difficult to quantify [4]. In addition to accuracy and measurement-independency considerations, direct use of imaging data without PNM simplification allows the quantification of uncertainties in terms of choices made on gray-scale intensity values.

Experimental uncertainties are often expressed as an error bar. Computational physics results, however, are further challenged with coming up with an error bar due to the much greater number of parameters involved [5,6]. Many numerical tools never pass the validation and verification phase. An early study illustrated where computational tools are used to quantify the uncertainties in experiments, which in turn confine the parameter space of the numerical domain [7]. In this study, we illustrated how a highly interactive and seemingly subjective task, such as image segmentation, can have its uncertainty quantified.

SAMPLES AND METHODS

Four samples were selected from a 40m interval of reservoir sandstone noted for a pore-lining interstratified chlorite/smectite clay mineral that affected various petrophysical properties including permeability and electrical conductivity. The mineralogy of this interval was 60-70 wt% quartz, 15-20 wt% feldspars, mostly Na-plagioclase, and 10-15 wt% clay minerals, mostlly authigenic chlorite/smectite. Diagenetic siderite cement occluded some of the pores in these samples. Routine core measurements revealed a high porosity sandstone with a range of permeability values (Table 1). Sample D was selected to represent the lower range of porosity and permeability observed in this interval. The actual mini-plug cut from the sample D interval cut through a tight stringer of rock where all of the visible pore space was filled with the siderite cement and therefore was not representative of the larger core plug used for original petrophysical properties.

Table 1. Basic petrophysical properties.

Sample	Analysis ID	Porosity	Permeability (mD)	Grain Density (cm3/g)	MICP Median Diameter (microns)
A	D0000450: 2µm D0000452: 4µm	0.144	3.1	2.68	0.8
B	D0000465: 2µm D0000466: 4µm	0.175	58.5	2.69	6.8
C	D0000467: 2µm D0000468: 4µm	0.159	23.4	2.68	5.8
D	D0000469: 2µm	0.070	0.5	2.66	

	D0000470: 4µm				

Low-field NMR relaxation measurements show a broad distribution of pores for the three samples with viable porosity (Figure 1). Conventional interpretation of these T_2 relaxation time distributions indicate that the large component faster than 10-20 msec corresponds to micro-porosity while the slower component represents the larger macro-porosity. The conversion of relaxation to pore dimensions requires the linear correlation term that represents the surface relaxivity [8]. Surface relaxivity values of 10 to 50 microns sec^{-1} were determined in an earlier study.

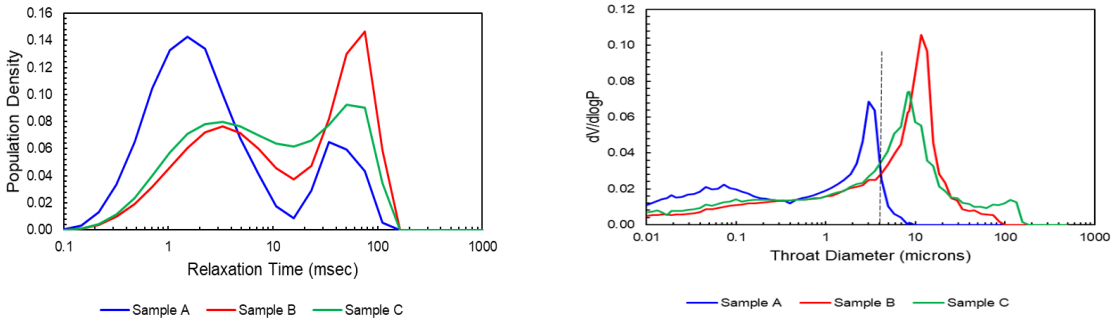

Figure 1. NMR T_2 relaxation time distributions show predominantly bi-modal distribution of pore sizes. MICP throat size distributions for samples in this study. Vertical dashed-line represents the 4-micron resolution of the microCT images.

Mercury injection porosimetry measurements were acquired on samples A-C with an AutoPore 9220 (Micromeritics) set up to acquire data between 0.5 and 60,000 psi. Throat size distributions generated from the Hg/air drainage curve showed that for these samples the dominant throat size was in the range of the resolution of the microCT images (Figure 1). The distributions were predominantly uni-modal, though sample A had the suggestion of a second mode of much smaller throat sizes than the dominant mode. Note that the modal throat diameter was larger than the median size reported in Table 1.

Mini-plugs, 4.0 mm in diameter and 6-8 mm in length, were drilled from core material adjacent to where the original routine core plugs were taken. The plugs were cleaned and dried. MicroCT images were collected in the dry state on a Versa 510 instrument (Zeiss) to acquire 4.0- and 2.0-micron resolution images. The absence of images acquired at different saturation states limited the detection of sub-resolution features [9]. The images were processed with the instrument's software and exported in *.tiff format. The total image package consisted of 1000 stacked images in the Z direction, 992 by 1014 voxels in the X and Y directions. These image stacks were cropped to 400x400x400 and 680x680x900 volumes to remove edge effects and poor-quality images at the ends of the sample. The cropped volumes were centered on the sample's center such that the middle slice for each cropped volume matched.

The cropped images were segmented with a Machine Learning engine optimized for a proprietary image-management cloud [9]. Specifically, a random forest algorithm was used. The workflow started with a set of seed voxels selected from the image's 2D training area that represented the pores and grains. In addition to gray-scale intensity and its gradient, a basket of statistical features was computed on the training data that included first and second derivatives of intensities, along with sensitivity information on the size of the neighborhood and edges. Iterative refinement of the seed voxels on the small training image ensured all important features were identified and correctly segmented. The segmentation procedure used on the training image was then automatically applied to the full 2D field of view and subsequently to the full 3D stack. The training image can cross multiple 2D images at different locations and orientations. A high-performance computing cluster was designed optimally for both such image processing and image-based numerical simulation [10].

Image resolution made it difficult to characterize sub-resolution pores associated with clay minerals. Consequently, a decision was made to combine the observable macro-pores with sub-resolution pores associated with the clay mineral lining for the purpose of this study. The highly subjective segmentation operation was repeated several times by two different operators with different backgrounds in geoscience and image processing. No effort was attempted to constrain image segmentation with core-derived porosity and clay mineral abundance values.

A number of petrophysical properties were calculated from these segmented images using direct numerical simulations on the voxels [11-13]. A spatial distribution REV was calculated to confirm that the sample volumes were representative of the larger samples used for the conventional core measurements. The calculated properties included total volume fractions, pore size distributions, electrical conductivity (Ohm's law solved with finite volume method), effective permeability (Multiphase Darcy's equation solved with finite volume method), and mercury/air capillary pressure (Youngs-Laplace equation solved with a morphological method), with a workflow based upon a previous validation effort [10].

RESULTS

The results from the highest porosity – permeability sample were the focus of this analysis, but all samples had similar results. All of the quantitative segmentation results and subsequent simulations on these three samples were generated from ML-based segmentation. Sample B was characterized by CT intensities that ranged from 2000 to 10,000 units, dominated by a mode around 7000 and a distinct shoulder on the distribution around 4000. The operators had different strategies to select seed points for the ML-based segmentation of the low intensity pore space (Table 2). Some chose short traces with only a few voxels while other runs included a larger number of voxels. While

the mean intensity value for each run was roughly the same, the larger range of values sampled with the longer traces produced a slightly broader histogram of segmented pores (Figure 2).

Table 2. Seed properties for porosity in Sample B 4-micron resolution images

Run	Porosity	No. Traces	No. Voxels	Mean	Std Dev	Max	Min
118	0.103	2	35	3859	514	5154	2975
123	0.110	2	25	3985	703	4996	2931
128	0.132	3	137	3965	575	5625	1924

Subtle features (red arrow in Figure 2) representing pore throats closer to imaging resolution could only be picked up via iterative seeding. Also note all voxels to the right of the red dashed line in Figure 2 would be assigned as grain using a conventional threshold-based method.

Quantitatively, different segmentations resulted in different estimates of pore volume. Run 128 generated an image porosity of 0.132, higher than the 0.103 and 0.110 values for runs 118 and 123. The difference in segmentation of a larger pore volume was driven by a broader range of seed values, not the mean value of the selected voxels. It was apparent that additional seeding from Run128 increased segmentation accuracy (Figure 3).

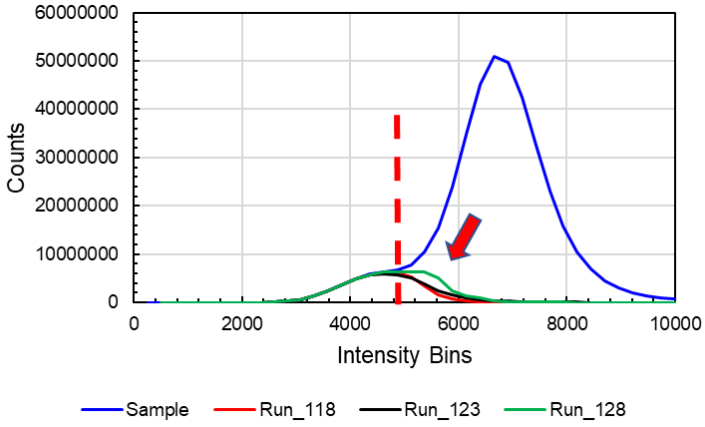

Figure 2. Histograms of segmented pores from different runs compared to the original sample intensity distribution.

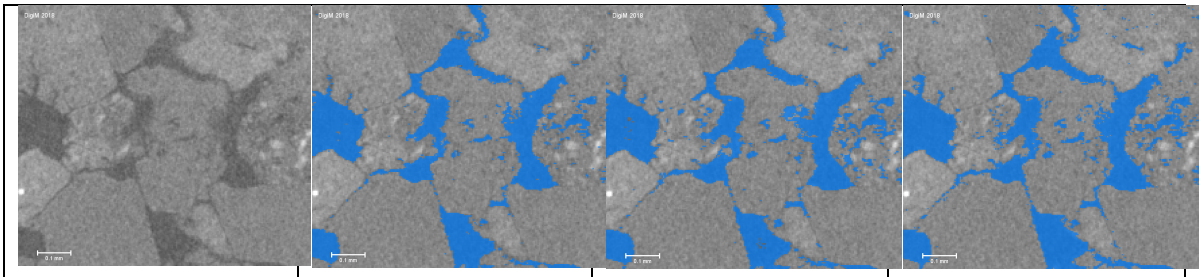

Raw CT	Run_118, phi=0.103	Run_123, phi=0.110	Run_128, phi=0.132

Figure 3. Comparison of Image Segmentation by various operators. Sample B, 4-micron resolution, 680x680x900 volume, slice 450.

In general, the image-based porosity value was 10-50% less than the value from routine core measurements. Image porosity for Sample B from different segmentation iterations ranged from 0.103 to 0.132, which was 59-72% of the total porosity of 0.175. The proportion of the T_2 distribution slow component was ~50% of the total signal intensity, which suggested that the image segmentation captured all of the larger pores.

The pore-size distributions generated from the microCT images were limited at the lower end by the resolution of the measurement. The different segmentation efforts did not generate large differences in calculated pore-size distributions. In large part this was due to the similarity in observed pore volume and the limited range of sizes detected by the microCT images. This was illustrated by the different segmentation runs on Sample B and their calculated pore size distributions. The two segmentation runs on 4-micron data set, runs 118 and 123, had no significant difference in the calculated pore-size distribution and the median size (Figure 4). The pore-size distribution associated with Run 128 captured some larger pores as the segmentation included more porosity. An additional segmentation run on the 2-micron resolution, small volume (400x400x400) had a distinct shift towards smaller pore sizes. The range of sizes was the same, roughly 1.5 orders of magnitude that illustrated how calculated pore size information was dependent upon image resolution. The limited range of observed pore sizes was illustrated by the calculated pore-size distributions for the three samples. Sample C had a distinctly smaller pore size that reflects the smaller grain size observed with this sample relative to the other two samples.

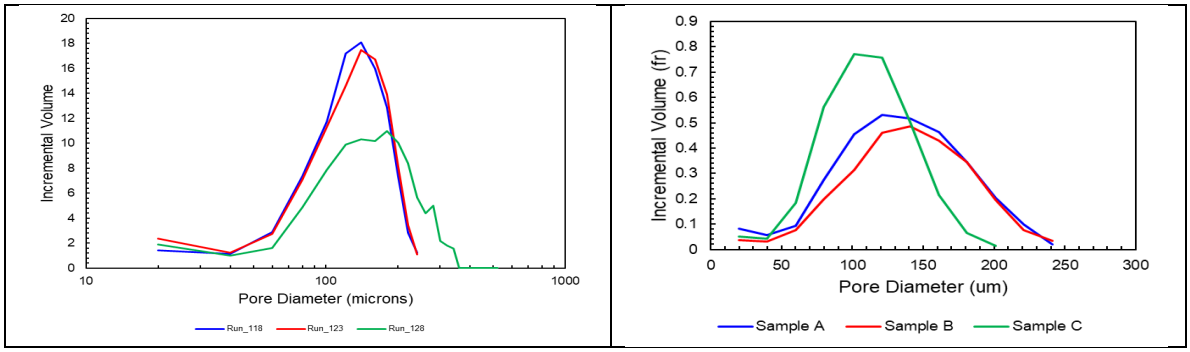

Figure 4. Comparison of pore-size distributions generated from different segmentation runs on 4-micron resolution images on Sample B (left) and for the three samples (right)

The overlay of the image-based pore-size distribution and the slow component of the T_2 distribution was observed for all samples and illustrated for Sample B (Figure 5). The MICP-based throat-size distribution was 1.5 orders of magnitude smaller than the pore-body sizes computed from microCT images.

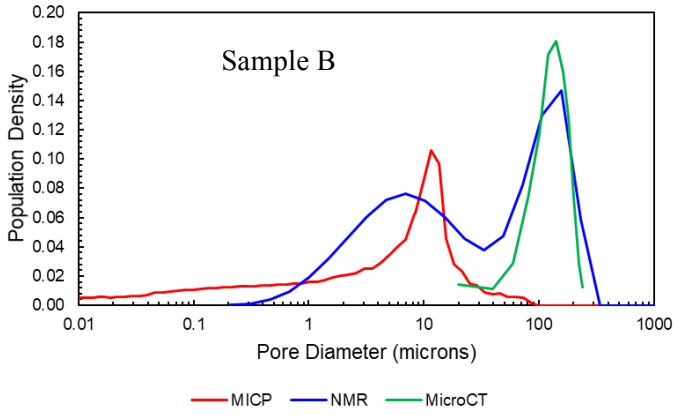

Figure 5. Comparison of image-based pore-size distribution for Sample B (4 micron resolution) with NMR and MICP results.

Calculation of transport properties was dependent upon the connected pore volume. Connected porosity values for each segmentation run for every sample in this study was > 90% of the total image porosity value. This was not affected by the size of the computed volume (680x680x900 versus 400x400x400) nor by the resolution of the image (4-micron vs 2-micron). The calculated permeability values were dependent upon the input permeability value for the porosity, which limited its value as a predictive tool since this starting value was somewhat arbitrary. The calculated permeability was slightly lower in the Z-direction than in the X and Y axes. No large-scale laminations were observed in the microCT images for Samples B and C that might create anisotropic flow patterns. In contrast, Sample A had distinct cementation patterns perpendicular to the Z-axis that reduced calculated permeability by a factor of 2-3.

Calculated electrical conductivity values were converted into Formation Factor by normalizing against the input conductivity value for the porosity. The resultant Formation Factor and image porosity determined the cementation exponents for these samples to be between 1.9 and 2.5. Replacing the total image porosity with connected image porosity reduced the scatter of points around a cementation exponent of 2.0. In general, the calculated conductivities for Samples B and C were higher in the Z-direction than in the X and Y, though the increase was less than 10%. Sample A with its distinct cementation pattern was less conductive in the Z-axis by a factor of 2.

Calculated MICP curves for these samples illustrated the limitations of IBRP methods. The small range of pore sizes and explicitly resolved pore throats observed in the 4-micron resolution images was reflected in the range of calculated pressures in the Hg/air system (Figure 6). The calculated MICP curve for Sample A did not begin to match the measured entry pressure, in large part due to most of the pores (and throats) being smaller than the resolvable pores in the microCT images and the presence of significant pore-filling cement. The somewhat larger pores and throats in Sample C generated a calculated entry pressure that was more agreement with the measured MICP curve, but the absence of small pore information limited its value at higher capillary pressures. Only with Sample B did the observed porosity system generate a MICP curve that showed good agreement with the measured results, and even there the low Sw behavior was incomplete. Calculations with the 2-micron resolution images were no better in that while they included smaller pores and throats, higher pressures, they lost information with the larger pores.

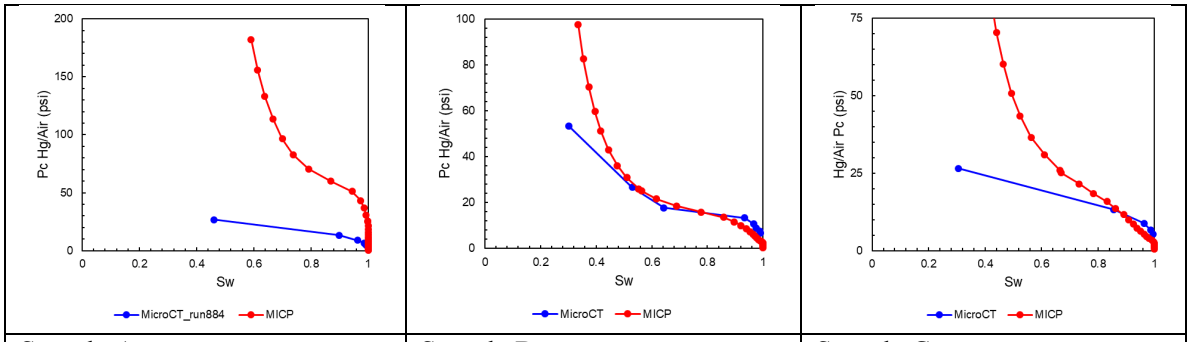

Sample A	Sample B	Sample C

Figure 6. Comparison of mercury capillary pressure curves generated from experiment (red) and image-based calculations (blue) for the low permeability (A), high permeability (B), and intermediate permeability (C) samples.

Several steps to evaluate uncertainty of resolvable intergranular porosity were followed in this study. Evaluation of the uncertainty of the micro-porosity was compounded by the absence of higher resolution data such as those obtained with scanning electron microscopy or synchrotron tomography, that made it much harder to quantity. This study also chose not to separate intergranular porosity from micro-porosity by using an

independent estimate of porosity partitioning such as can be extracted from the NMR relaxation measurements. While this second approach to evaluate the uncertainty associated with distinguishing two types of porosity has its adherents, the choice here was to focus on a combined porosity distinct from the grains.

This project assumed fixed imaging resolution, image preprocessing, segmentation post-processing and simulation, and that no true reference value existed for the ML segmentation. The focus in this study was on image segmentation of intergranular porosity and the uncertainties generated by threshold segmentation and supervised ML segmentation in identifying intergranular porosity.

In contrast, a global threshold segmentation approach incrementally changed the intensity segmentation threshold to match the core-based porosity, which defined a variation threshold (i.e., 5% from the known porosity). The corresponding intensity value normalized by the threshold intensity value produced an error bar [12]. Since the ground truth porosity value remained unknown, a directional derivative model was employed.

Porosity was calculated with varying threshold gray-scale values that ranged between 4000 to 7000 for the 4-micron resolution images of Samples A, B and C. An increased threshold value improved the resolution of the intergranular pore space for Sample B, but at the expense of adding a significant contribution of single-voxel pores within the grains (Figure 7). As a reference, the gray-scale range of the grain phase based on a single quartz particle was between 4200 and 8500, with a standard deviation of 1230. The gray-scale range of pore phase on a selected intergranular pore was between 2300 and 5700, with a standard deviation of 980.

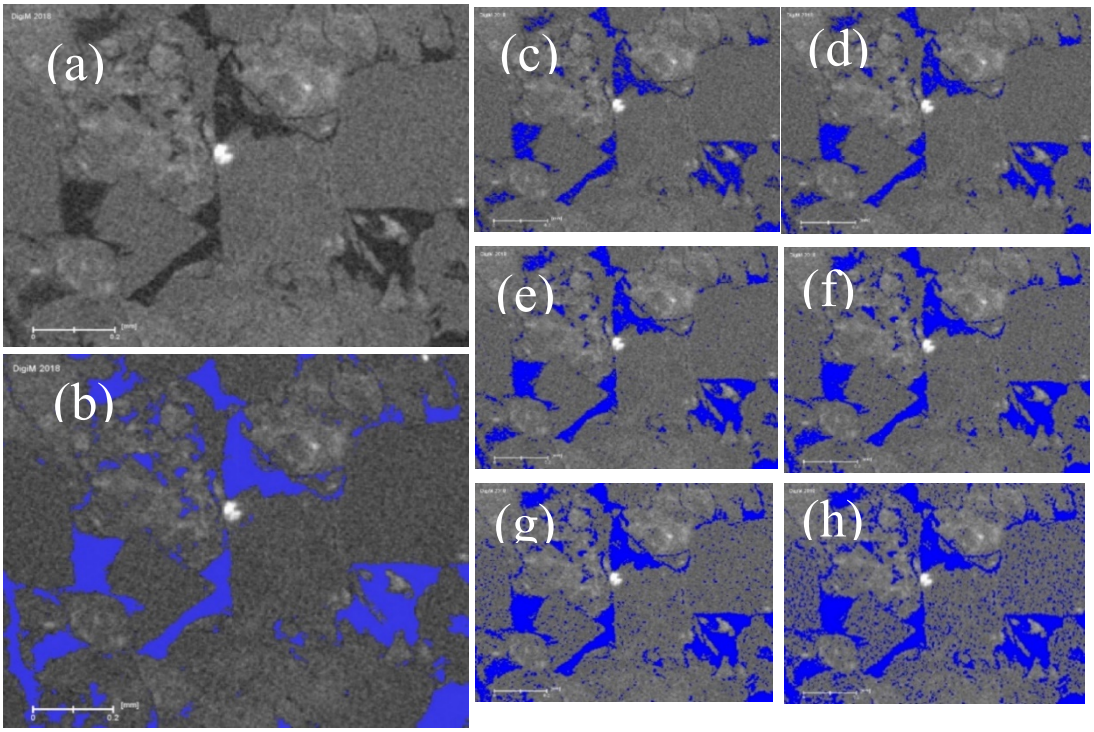

Figure 7. ML segmentation versus threshold segmentation for Sample B, 4-micron resolution images. (a). Gray-scale image with intensity range 945-15000. (b). Machine learning segmentation, run128. (c). Threshold 4500. (d). Threshold 4800. (e). Threshold 5100. (f). Threshold 5400. (g). Threshold 5700. (h). Threshold 6000.

The comparison of resolved porosity as a function of threshold value indicated two linear slopes, a lower slope at gray-scale value of 5200 or smaller (line 1), the other higher slope at gray-scale values of 6200 or higher (line 2) (Figure 8). The gray-scale values between 5200 and 6200 represented the uncertainty zone for threshold segmentation. The intersection of the two linear slopes anchored a normal to the intensity threshold curve, which intersected with the intensity threshold curve at point 3. The tangential slopes 1 and 2 deviated from the curve at point 4 and 5 respectively. Points 3, 4 and 5 defined the threshold porosity, and its upper and lower limits (Table 3).

The threshold values measured with this method agreed well with the core porosity value. However, this good agreement was misleading since the goal of this thresholding exercise was to segment out intergranular porosity. The good agreement indicates that the threshold segmentation is effective in estimating a bulk porosity with averaged effect from micro-porosity, but erroneous in defining the distribution of the porosity. Consequently, using this segmentation to make any rock physics study is risky at best, and wrong most often. Micro-porosity has distinctive physical properties that has to be treated differently. This is reflected by the large range of uncertainties for all three samples.

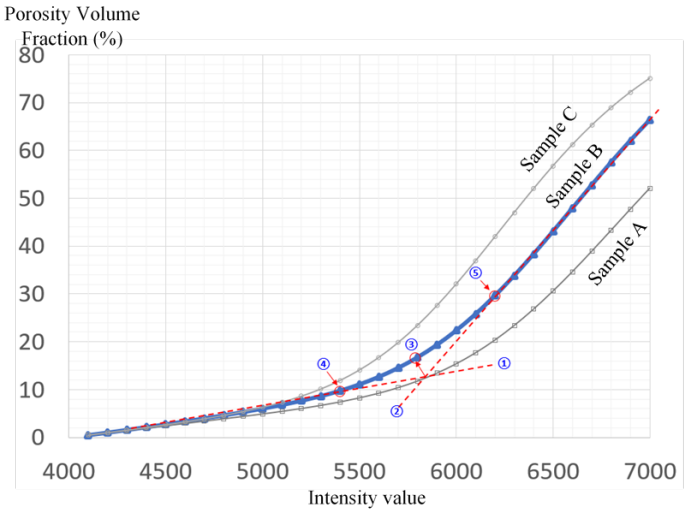

Figure 8. Relationship between image porosity and intensity for all three samples.

The computation of ML-based segmentation resulted in a statistical probability for each voxel. This probability function was used to estimate uncertainties from ML segmentation. These results illustrated how ML segmentation reduced uncertainty, particularly on the boundary between intergranular porosity and mineral grains. Uncertainties were slightly larger when differentiating intergranular porosity from micro-porosity.

Table 3. Porosity and its uncertainties assessed with the proposed framework

Sample ID	Method	Porosity	Lower Limit	Upper Limit
A	Threshold	0.14	-0.06	+0.15
A	ML	0.10	-0.01	+0.01
B	Threshold	0.16	-0.07	+0.11
B	ML	0.13	-0.03	+0.02
C	Threshold	0.15	-0.05	+0.15
C	ML	0.11	-0.01	+0.02

It is also important to note that the reference value was also subjective to the particular workflow. The segmentation strategy can be very different for inter-granular porosity characterization and for multi-scale upscaling. In the latter case, for example, porosity phase will need to be segmented into a volume fraction that is higher than the total porosity, to allow higher resolution properties to be distributed.

DISCUSSION

An outstanding challenge of IBRP is its uncertainty associated with various steps in the process, which limits its adoption for practical engineering decision-making. Lack of systematic effort to quantify uncertainty, and sometimes even recognize the importance

of uncertainty, further underscores the gap that needs to be filled by the research and development community. In this project, a set of shaly-sand samples with significant amount of authigenic chlorite/smectite that lined the larger pores was tested to identify uncertainty quantification (UQ) requirements associated with image-processing steps. We focused on segmentation in particular, with two operators using two popular segmentation methods.

Images from a conventional microCT are limited in the range of features that can be extracted. In this study the size range was less than 2 orders of magnitude. The lower limit was defined by image resolution of the instrument and the upper limit controlled by sample size. Even with these constraints, the image volumes in this study contained ~$2*10^5$ pores, which was sufficient to provide a statistical representation of pores in these samples. The significant clay mineral volume found lining the pores of these samples has a major impact on petrophysical properties because of its high surface area and interparticle porosity yet could not be evaluated in this instance due to the limitations in the images. The strategy in this exercise was to focus on the larger intergranular porosity and to leave the micro-pores associated with the clay minerals to a later study.

Threshold segmentation can mis-leadingly reach porosity matching the core analysis data. The petrophysical properties derived therein, however, will be completely erroneous. The uncertainty framework presented in this paper reflected the large, over 100% uncertainty.

ML segmentation limits uncertainty to 30% or lower. The impact of individual operator can also be quantified, which is within the 30% uncertainty range. It clearly offers more flexibility and does a better job dealing with pore-grain interfaces.

It is important to emphasize that segmentation is only one step among many in IBRP workflow. The uncertainty of the workflow strongly dependent upon image quality, image modality, image filtering/pre-processing, segmentation post-processing, and the numerical simulation technique. As the value of imaging is dictated by resolution, in order to extend the pore size information from image-based methods in order to match the 3-4 order of magnitude range associated with NMR methods, other imaging tools must be added.

REFERENCES

[1] Schembre-McCabe, J., Kamath, J., “Using digital rock technology to quality control and reduce uncertainty in relative permeability measurements,” *Proceedings of the 2017 International Symposium of the Society of Core Analysts*, Vienna (2017) SCA 2017-014.

[2] Idowu, N., Nardi, C., Long, H., Øren, P., Bondino, I., "Improving digital rock physics predictive potential for relative permeabilities from equivalent pore networks", *Proceedings of the 2013 International Symposium of the Society of Core Analysts*, Napa Valley, (2013), SCA2013-017.

[3] Schembre-McCabe, J., Salazar-Tio, R., Ball, G., and J. Kamath, "A framework to validate Digital Rock Technology," *Proceedings of the 2011 International Symposium of the Society of Core Analysts*, Austin (2011), SCA 2011-028.

[4] Idowu, N., Nardi, C., Long, H., Varslot, T., and Oren, P., "Effects of segmentation and skeletonization algorithms on pore networks and predicted multi-phase transport properties of reservoir-rock samples", *Jour. Reservoir Evaluation & Engineering*, (2014) v.17, no. 4, pp. 473-83.

[5] Al-Taie, A., Hahn, H.K., Linsen, L., "Uncertainty estimation and visualization in probabilistic segmentation," *Computers & Graphics*, (2014) v. 39, pp. 48-59.

[6] Wu, J.C., Halter, M., Kacker, R.N., Elliott, J.T., Plant, A.L., "Measurement uncertainty in cell image segmentation data analysis," (2013) *NIST Internal Report 7594*, https://dx.doi.org/10.6028/NIST.IR.7954

[7] Zhang, S., Zabusky, N.J., Peng, G., and Gupta, S. Shot gaseous cylinder interacytions: Dynamically validated initial conditions provide excellent agreement between experiments and numerical simulations to late-intermediate time. Physics of Fluids. (16) 5, May 2004, pp1203.

[8] Dunn, K-J., Bergman, D., and LaTororraca, G., "Nuclear Magnetic Resonance: Petrophysical and Logging Applications, (2002) Pergamon Press, Amsterdam.

[9] Lezoray, O., Charrier, C., Cardot, H., and Lefevre, S. (Eds) "Machine Learning in Image Processing" *EURASIP Journal on Advances in Signal Processing*. 2008:927950, 2008.

[10] Long, H., Nardi, C., Idowu, N., Carnerup, A., Oren, P., Knackstedt, M., Varslot, T., and Sok, R., "Multi-scale imaging and modeling workflow to capture and characterize microporosity in sandstone", *Proceedings of the 2013 International Symposium of the Society of Core Analysts*, Napa Valley, CA (2013), SCA 2013-013.

[11] DigiM I2S, http://www.digimsolution.com/products/enterprise-solution/ (2018)

[12] Byrnes, A., Zhang, S., Canter, L. and Sonnenfeld, M., "Application of integrated core and 3D image rock physics to characterize Niobrara chalk properties including relative permeability with bound water effect", *Proceedings of the 2017 Unconventional Resources Technology Conference*, Austin (2017), URTeC 2670963.